

Flow Visualization in Artificial Porous Media from Microfluidic PMMA Devices

D. S. Park¹, S. King¹, K. E. Thompson², C. S. Willson³, D. E. Nikitopoulos¹

¹Department of Mechanical Engineering, ²Department of Chemical Engineering, ³Department of Civil and Environmental Engineering, Louisiana State University, Baton Rouge, LA, USA

ABSTRACT

Microfluidic polymethylmethacrylate (PMMA) devices for study of particle transport in artificial porous media were designed and microfabricated using hot embossing with a brass mold insert containing a microchannel network with eight layers. After thermal bonding to enclose the microchannel network, a process protocol was applied to successfully remove bubbles in the PMMA device. Characterization protocols were developed for study of fluorescent particle tracking, accumulation, and retention in these microfluidic chip artificial porous media. Particle accumulation and retention was observed throughout the microfluidic network domain and predominantly at the inlet section of the PMMA device due to entrance effects. Particle Image Velocimetry of the PMMA device allowed for generating velocity profiles in the chip microchannel networks.

INTRODUCTION

Visualization of the flow in the artificial porous media is important [1-5] because it allows for correlation of the observed flow patterns from the artificial porous media to physical and fluid properties of real reservoir materials including sandstone, carbonate, and fractured rocks. A common approach to make the artificial porous media is using glass beads packed in a confined space for experimental investigation of flow patterns [2], but it limits the control of flow geometries of the porous media such as converging-diverging channels, splitting and rejoining channels, and a distribution of channels sizes. Microfabrication of silicon/glass [4,6] can be used for fabrication of artificial porous media through well-established techniques of metal deposition, photolithography, and etching for multiple layers, but this process carries the drawbacks of high material and process costs.

In this paper, a 2.5D artificial porous medium was designed with random bifurcation and re-combination geometries and cross-sections, and microfabricated in polymethylmethacrylate (PMMA) using hot embossing. This process is relatively inexpensive compared to fabrication in silicon/glass and allows for production of multiple chips through replication at low cost after fabrication of a mold insert [7, 8]. The PMMA devices were used for development of characterization protocols to study particle tracking,

accumulation, and retention with fluorescent nanoparticles as tracers in artificial micro-chip porous media.

DESIGN

The prototype design of a 2.5D artificial porous medium involved a network of 2,500 channels (throats) with different widths and depths, and was based on the design used by Crandall et al. [9] after applying anisotropic scaling. Eight different layers defining an equal number of different arbitrarily defined depths were deployed to provide a limited three dimensional component of the geometry. The resulting 2.5D geometry, although not entirely consistent with the heavily 3D pathways of actual rock samples, makes three dimensional motion of the fluid and the target nanoparticles possible. The prototype design for the artificial porous medium device (50 by 50 channels, square footprint of 101.6 mm by 101.6 mm, Figure 1) had eight different layers (Figure 1(b): L_{DG} (dark gray layer) being the top layer in the polymer chip with L_M (magenta layer), L_B (blue layer), L_C (cyan layer), L_G (green layer), L_Y (yellow layer), L_R (red layer), and L_{LG} (light gray layer)) with a minimum channel width of 0.2 mm and maximum channel width of 1.0 mm and uniform distribution channel widths. The dimensions for each layer of the prototype were summarized in Table 1.

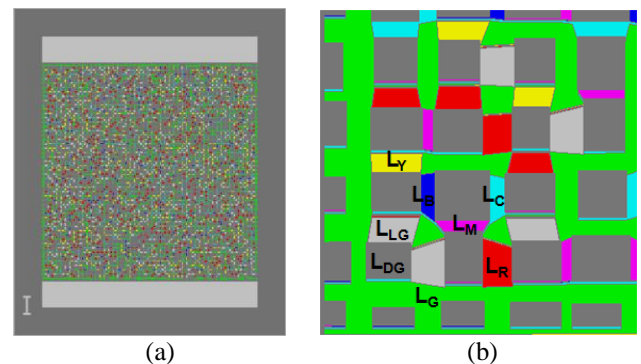


Figure 1: Schematic diagrams of a porous medium for (a) overall view and (b) close-up view of left inlet section showing eight microchannel network layers (L_{DG} (dark gray layer), L_M (magenta layer), L_B (blue layer), L_C (cyan layer), L_G (green layer), L_Y (yellow layer), L_R (red layer), L_{LG} (light gray layer)).

The prototype design of a 2.5D artificial porous medium was subject to anisotropic scaling; the widths were scaled down by a factor of $\frac{1}{4}$ and the depths by a factor of $\frac{1}{12}$. The summary of the depths for the each layer on the mold insert (L_{DG} to L_R) and those anticipated on the molded polymer (L_M to L_{LG}) is provided in Table 2. The design of the full footprint (38 mm by 58 mm) of the device in Table 2 was rendered for fabrication of a mold insert, including ports for fluidic inlet

Table 1: Summary of dimensions of a prototype 2.5D artificial porous medium.

Width range (mm)	Layer	Depth (mm)
1.0-0.885	L_{LG}	0.9652
0.885-0.771	L_R	0.8636
0.771-0.657	L_Y	0.7112
0.675-0.543	L_G	0.6096
0.543-0.428	L_C	0.4572
0.428-0.314	L_B	0.3556
0.314-0.2	L_M	0.2032
	L_{DG}	0

Table 2: Summary of dimensions of an anisotropically scaled 2.5D artificial porous medium (chip: polymer chip; MI: mold insert).

Width range (μm)	Layer	Chip (μm)	MI (μm)
250-221	L_{LG}	47	0
221-193	L_R	41	6
193-164	L_Y	34	13
164-136	L_G	29	18
136-107	L_C	22	25
107-79	L_B	17	30
79-50	L_M	11	36
	L_{DG}	0	47

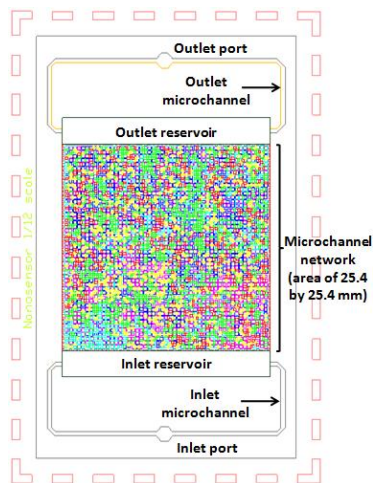


Figure 2: Design layout of the full footprint 2.5D artificial porous medium device.

and outlets, reservoirs, and fluidic distribution channels (Figure 2) using AutoCAD (San Rafael, CA, USA). The artificial porous medium portion with a microchannel network for random bifurcation and re-combination geometries and cross-sections was designed on a 25.4 mm by 25.4 mm square area. The channel widths were from 50 to 250 μm with various depths in eight separate layers (L_{DG} to L_{LG} , Table 2).

MICROFABRICATION

A brass mold insert containing the design shown in Figure 2 was micro-milled (KERN MMP-2522, KERN Micro Feinwerktechnik GmbH, Eschenlohe, Germany) using 50 μm diameter milling tools. First the layers for reservoirs (45° taper for better de-molding and smooth transition of fluids) and fluidic distribution channels were micro-milled, followed by micro-milling of L_R down to L_{DG} . The micrograph of Figure 3(a) from scanning electron microscopy (SEM) inspection showed the clear formation of separate layers and rounding effects at the corners of the features due to the milling bit radius.

The 2.5D artificial porous medium in the brass mold insert was hot embossed on PMMA substrate. PMMA sheets (2.6 mm thick) were cut into 6-inch pieces and placed in a convection oven at 80°C for 12 h to dehydrate the stock material prior to micro-molding. Hot embossing was done using a commercially-available hot embossing machine (HEX02, Jenoptik Mikrotechnik, Jena, Germany) using the brass mold insert. A molding force of ~ 22 kN was applied to the polymer part for 3 minutes at a mold temperature of 162

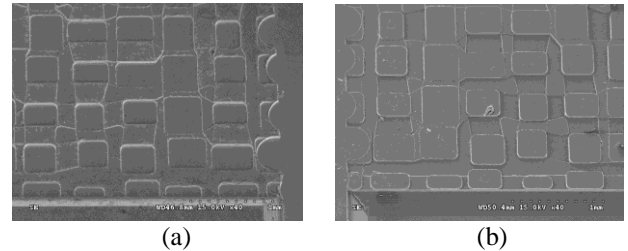


Figure 3: SEM images of (a) inlet section of a brass mold insert and (b) corresponding inlet section of a PMMA device.

Table 3: Summary of metrology results on depth profiles for eight different microchannel network layers in a PMMA device before/after TFB process.

Unit (μm)	Design	Before TFB	After TFB
L_{DG}	0	0.0	0.0
L_M	11	4.1	3.9
L_B	17	15.7	13.8
L_C	22	20.1	19.2
L_G	29	30.7	27.6
L_Y	34	33.8	31.9
L_R	41	43.7	39.9
L_{LG}	47	45.0	40.7

°C with a de-molding temperature of 105 °C. The SEM inspection of hot embossed PMMA showed clear micro-milling marks on the channel surfaces indicating that the embossing was successful with complete filling (Figure 3(b)).

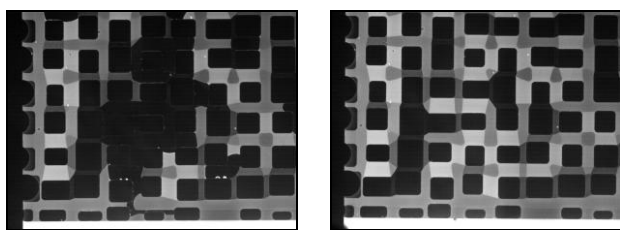
Once cleaning of hot embossed PMMA chips [10] and generating fluidic through-holes (1 mm diameter) were done, the device was sealed with a thin PMMA sheet (250 μm thick) through thermal fusion bonding (TFB). The metrology on the depth profiles was carried out by a non-contact profilometer (Nanovea ST400, Micro Photonics Inc., Allentown, PA, USA) to evaluate the deformation from TFB. The departure from design dimensions was as small as 0.2 μm for the shallowest layer in L_M and as large as 4.3 μm for deepest layer in L_{LG} (Table 3).

After completing the metrology studies, several 2.5D micro-models were prepared and fitted with inlet and exit port fittings for fluidic interconnects using nanoport assemblies (N-333, Upchurch Scientific, Oak Harbor, CA, USA).

FLUIDIC EXPERIMENTS

A pressure test was conducted to qualify the bond strength between the cover and the chip itself. The test indicated that the bond strength supports internal pressure up to 15 psig, which is more than adequate for the application at hand. Because the associated test is destructive, it was conducted only once in order to avoid wasting useful chips. Therefore the uncertainty band on the maximum pressure reported is unknown. Nevertheless, prior experiences from testing several other chips with different microfluidic patterns have given maximum operating pressure of the same order.

After completing the manufacture, metrology, and strength testing of the 2.5D micro-model design, injection tests were conducted to develop a protocol for the removal of bubbles upon filling the chip with water. The persistence of bubbles in complex flow domains, especially when using weakly wetting micro-model materials such as PMMA (contact angle of 65-70°), is a known issue. Although the presence of some bubbles in the chip during fluidic experiments should not in principle be a problem given the scope of the planned experiments, it was deemed desirable to eliminate them in the highest degree possible. During the bubble elimination protocol, different chip filling and flushing rates and durations were tested, resulting in the optimized bubble removal protocol by pulling water from inlet to outlet using a 30 mL syringe for ~12 hrs and then pushing water



(a) (b)

Figure 4: Images (2X magnification) at the inlet section of a PMMA device with Rhodamine dye B filled (a) before air bubble removal and (b) after air bubble removal.

from inlet to outlet by the same syringe at 10 μL/min for ~48 hrs using a syringe pump. Fluorescent microscopy inspection of the microchannel network with Rhodamine dye B confirmed the effective removal of air bubbles (Figure 4).

Preliminary particle flow experiments were conducted using fluorescence microscopy after flushing the dye with water, and injecting fluorescent nanoparticles (0.96 μm size, ~2.8 x 10⁸ particles/mL, neutrally buoyant polystyrene particles impregnated with a red fluorescent dye (R950), Duke Scientific Inc., Palo Alto, CA, USA) as tracers at a flow rate of 1.5 μL/min. The observation regions for the preliminary experiments are indicated in Figure 5, superposed on an SEM image of the corresponding region of the micro-model obtained before thermal bonding of the cover, together with local channel depth information. Representative images from this experiment are presented in Figures 6-8 including each of the observation regions as indicated in Figure 5. These images were obtained 2 hrs after the particle flow at the nominal flow rate (1.5 μL/min) was initiated. One of the principal observations from Figure 6 is that the most significant accumulation is observed at the transition from the



Figure 5: Observation locations from the left near-inlet region of the micro-model chip for the preliminary particle flow experiments. The table on the right codifies measured channel depths in the micro-model.

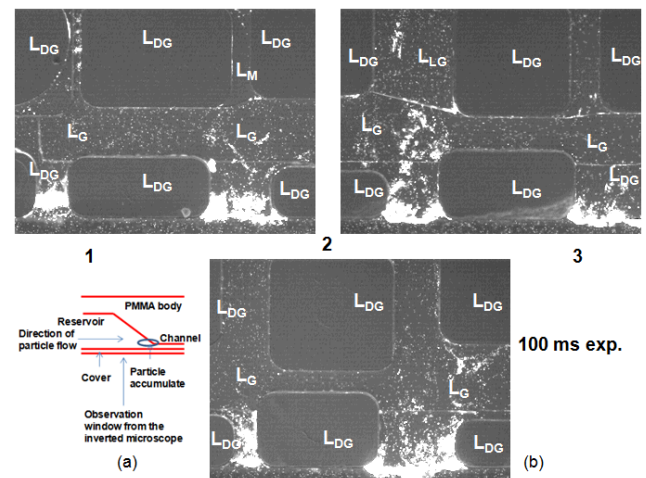


Figure 6: Images obtained during preliminary particle flow experiments, depicting the motion of particles and particle accumulation in the 2.5D artificial porous media micro-model acquired at observation fields of view (FOVs) #1, #2, and #3 as defined in Figure 5.

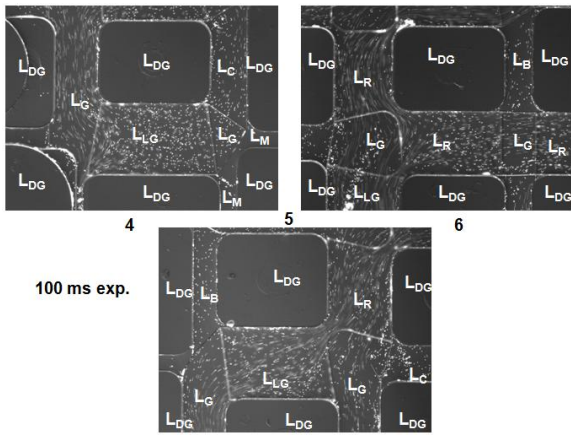


Figure 7: Images obtained during preliminary particle flow experiments, depicting the motion of particles and particle accumulation in the 2.5D artificial porous media micro-model acquired at observation FOVs #4, #5 and #6 as defined in Figure 5.

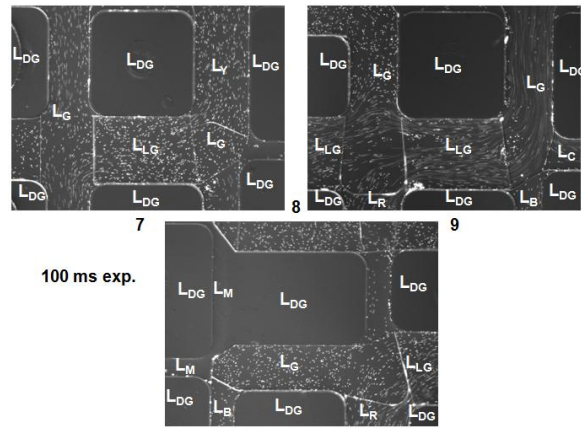


Figure 8: Images obtained during preliminary particle flow experiments, depicting the motion of particles and particle accumulation in the 2.5D artificial porous media micro-model acquired at observation FOVs #7, #8 and #9 as defined in Figure 5.

reservoir to the channel network, the principal location illustrated schematically in Figure 6a, where the shape of the transition from the reservoir depth to the initial network channel depth is also shown. The accumulation is significant to the extent of potentially clogging some of the entry vias (note that in FOV #1 there are visibly lower velocities in Figure 6b). Evidence of local accumulation initiation is also detected in the interior (see for example Figure 7 FOV #6; Figure 8 FOV #9).

Following the preliminary experiments, a new fluidic

experiment was designed to:

1. determine the extent to which deposition/accumulation of particles occurs and if there are preferred regions of such accumulation,
2. examine the degree to which these accumulations persist when subject to flushing,
3. obtain trial sets of images enabling preliminary quantification of the flow field at various locations on the micro-model channel network domain by applying micro PIV.

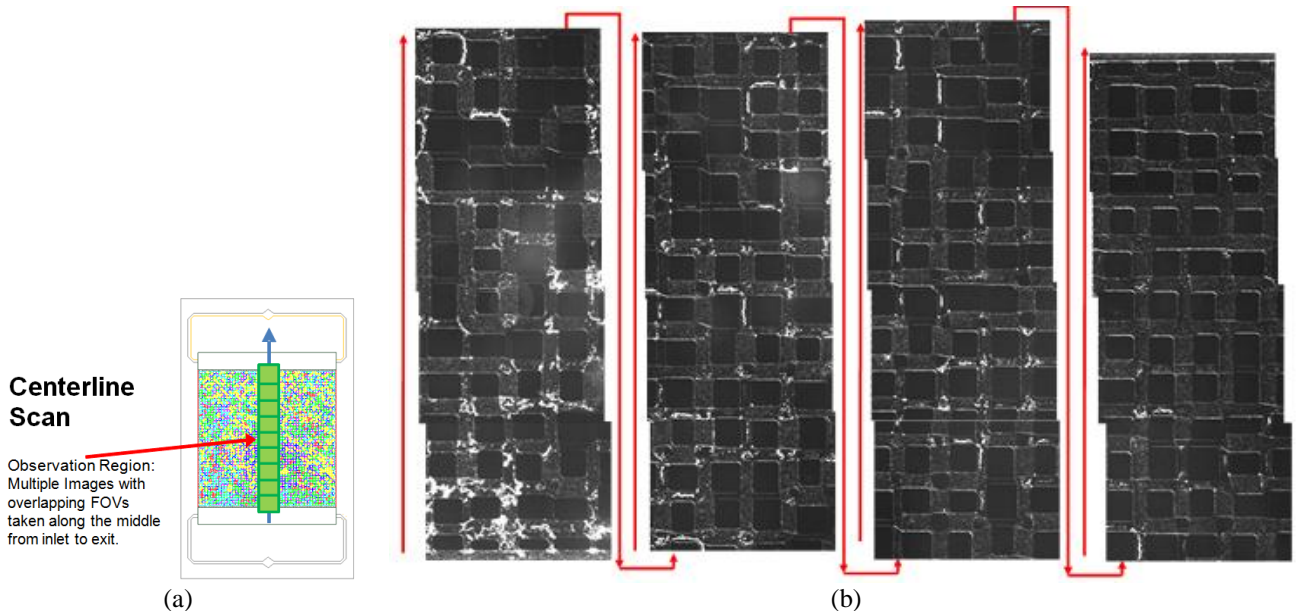


Figure 9: (a) Schematic illustration of the centerline scan path comprising of 16 partially overlapping FOVs along the centerline of the 2.5D artificial porous media micro-model chip in the bulk flow direction, and (b) Sixteen images with partially overlapping FOVs (as in Figure 5(a)) illustrating particle deposition and flowing particles from entrance (lower left corner) to exit (upper right corner) of the 2.5D artificial porous media micro-model. A 4X objective was used to acquire these images with exposure time 100 ms.

The experiment protocol included observation in specific parts of the micro-model chip along:

- the centerline from inlet to exit in the bulk flow direction (see Figure 9 for observation path),
- the inlet over half the width of the chip, across the bulk flow direction (Figure 10),
- a path immediately downstream of the inlet over half the width of the chip, across the bulk flow direction (Figure 11),
- the middle half-width of the chip, across the bulk flow direction (Figure 12), and
- the exit half-width of the chip across the bulk flow direction (Figure 13).

Observations along the centerline were made after 1.5 hrs from the initiation of particle flow at a flow rate of 1.5 $\mu\text{L}/\text{min}$, while for the rest, observations were made in three stages: 1.5 hrs after particle flow initiation, 24 hrs after particle flow initiation, and, following that, 24 hrs after switching to flushing the chip with particle-free de-ionized water at the same flow rate. The first two stages of observation were intended to qualitatively evaluate the rate of particle deposition/accumulation on a long time scale, and the last stage was intended to qualitatively examine the extent to which the particles deposited were “permanently” retained, and not a result of redistribution (i.e. particles temporarily trapped locally, swept away and replaced by a new progressive accumulation of new particles).

A survey of particle flow along the centerline of the micro-model chip is presented in Figure 9(b) through a sample set of images over all sixteen fields of view. Localized particle accumulation was observed throughout the centerline strip of the microfluidic network, more significant nearer to the inlet

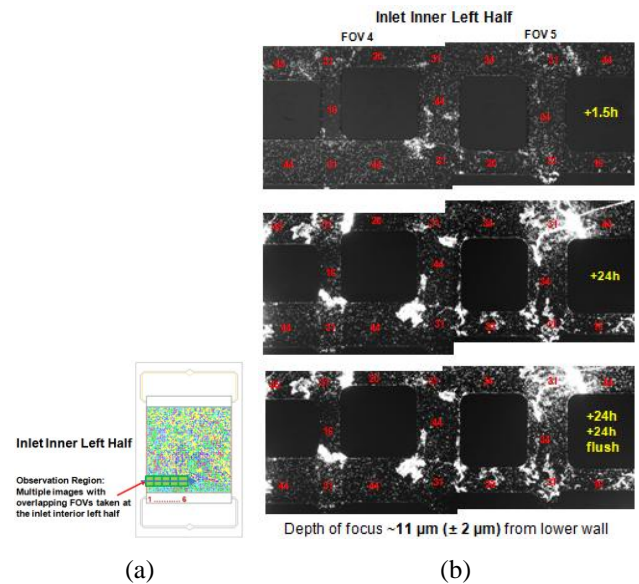


Figure 11: (a) Schematic illustration of the inlet inner left half scan path comprising of 6 partially overlapping FOVs along the inner left half of the inlet, and (b) Images from two consecutive FOVs (#4 and #5 per Figure 7(a)). A 10X objective was used to acquire these images with exposure time of 10 ms. Numbers in red indicate the channel depth.

and progressively less so further downstream. This immediately points to a potentially significant dilution of the particle concentration occurring in the neighborhood of the inlet which may be responsible for the reduced localized accumulation observed further downstream. This may necessitate experiments with different initial concentrations of

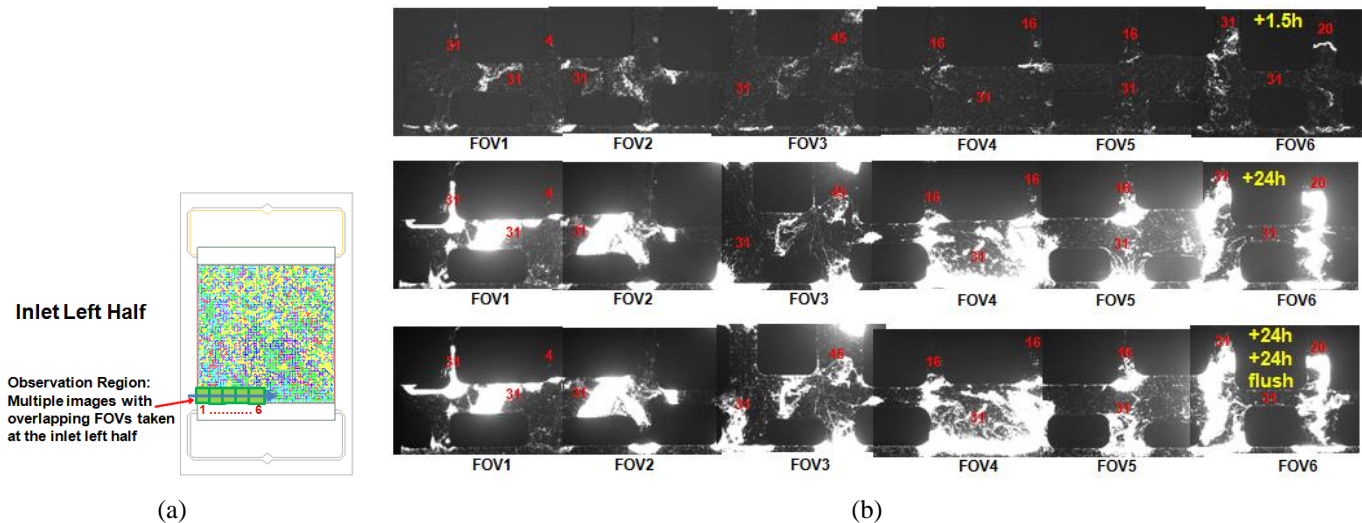


Figure 10: (a) Schematic illustration of the inlet left half scan path comprising of 6 partially overlapping FOVs along the left half of the inlet of the 2.5D artificial porous medium micro-model chip across the bulk flow direction, and (b) Images from all consecutive FOVs (per Figure 6(a)) from the inlet left half region of the 2.5D artificial porous medium micro-model, obtained during the particle flow/deposition/retention experiments. Top-to-bottom, are views obtained 1.5 hrs after particle flow was initiated, 24 hrs after particle flow was initiated, and 24 hrs after reverting to a particle-free flush at the same flow rate. Flushing was started after 24hrs of particle flow. A 10X objective was used to acquire these images with exposure time of 10 ms. Numbers in red indicate the channel depth.

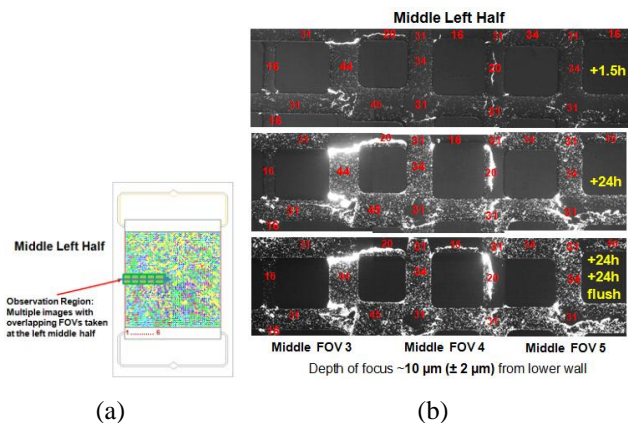


Figure 12: (a) Schematic illustration of the middle left half scan path comprising of 6 partially overlapping FOVs, and (b) Images from three consecutive FOVs (#3, #4 and #5 per Figure 8(a)) from the middle left half region. A 10X objective was used to acquire these images with exposure time of 10 ms. Numbers in red indicate the channel depth.

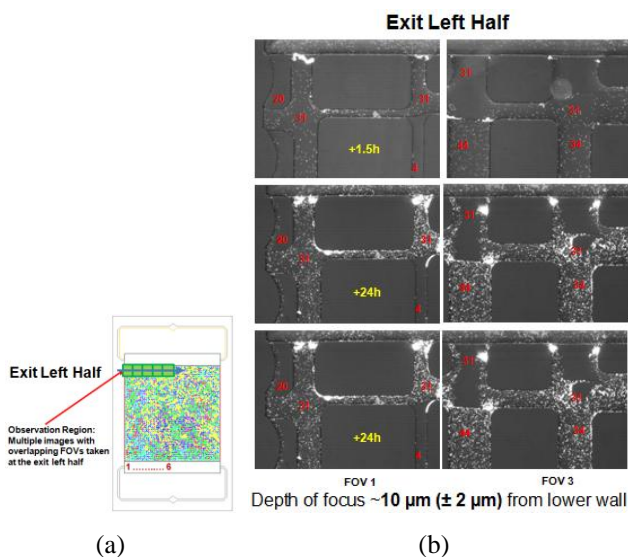


Figure 13: (a) Schematic illustration of the exit left half scan path comprising of 6 partially overlapping FOVs, and (b) Images from two FOVs (#1, and #3 per Figure 9(a)) from the exit left half region. A 10X objective was used to acquire these images with exposure time of 10 ms. Numbers in red indicate the channel depth.

particles. Another immediate observation from the bird's-eye centerline view is that string-like accumulations occur throughout the observed domain.

Accumulations of particles at the inlet presented in Figure 10 are observed from early on (1.5 hrs) at the inlets from the reservoir to the channel network as well as in the interior horizontal channels and the transitions from deeper ($31 \mu\text{m}$) to the shallower channels. These accumulations grow significantly over 24 hrs to the extent of clogging some of the vias completely. These accumulations are undiminished over the 24 hr flush, indicating that they are fairly stable, albeit

some smearing of deposited/accumulated particles can be seen. In addition to the localized accumulations, the evidence from the images after flushing indicates that there is also individual particle deposition and entrapment on the walls of the channel network. This is documented in the images from the other observation stations as evidenced in Figures 11, 12, and 13. Streak-like structures of deposited particles are also detected some of them resembling particle path lines. These structures are as of yet unexplained.

The evidence from Figures 11, 12, and 13 also documents accumulation of particles in transitions from deeper to shallower channels in the flow direction, this flow direction having been identified by cinematic observations. Deposition/accumulation of particles on the side-walls as well as the top and bottom walls is evident at all stations (Figures 11, 12, and 13). Accumulations of particles also occur in regions of stagnant flow at multi-channel junctions (see for example the top part of FOV #5 in Figure 11, and the lower part of FOV #3 in Figure 12).

The distinct particle accumulation lines observed along the length of shallower channels are evidence of some depth non-uniformity of high-aspect ratio shallow channels. This non-uniformity is evident in the fluorescent dye tests (see Figure 4(b)) where careful inspection reveals span-wise fluorescence non-uniformities in several channels. Typically the center of these channels in Figure 4(b) appears darker than near the side-walls, indicating a diminished depth at the center. In such case the available flow area is larger close to the side-walls allowing more flow to go through compared to the center where the available flow area is more restricted. Thus particles flow into these channels of non-uniform cross-section preferentially nearer to the side-walls and get deposited primarily towards the shallower central region where the convection is diminished. This accumulation results in the progressive sealing off of the central part of the channels further promoting the accumulation along a line aligned with the length of the respective channels. It should be noted that the same would occur if these shallower channels were collapsed. However, the dye filling test reveals that they are not.

Examples of such linear accumulations are found upon inspection in Figure 9(b) and Figure 12. Most of them are one-sided, i.e. the accumulation is observed close to one of the side-walls only. This is not surprising given the complexity of the interconnected channel network, which creates regions of broadly varying velocities along distinct paths and "rivers" along paths of least resistance. Therefore, the flow through these channels of non-uniform span-wise depth may well prefer one side over the opposite one if that would constitute the path of least resistance depending on the pressure distribution at the respective channel entrance. On occasion, preferential accumulation near channel side-walls occurs on both sides when the channel is of higher aspect ratio (see for instance Figure 13 at the channel network exits into the outlet reservoir).

Preferential local accumulation of particles can also be caused because of wall-surface non-uniformities such as wettability or roughness (the latter may be responsible for the former if it is on the nanometer scale), but for the moment this

cannot be verified. It would require surface metrology on a smaller scale than what has been conducted. Without discarding this probable cause, there is good evidence that hydrodynamic effects are significantly responsible for the localized accumulations of particles, and knowledge of the local flow-field can explain some of these localized accumulation observations.

Because at the scales of this micro-model and the particles used, the hydrodynamics are likely to play a defining role, a preliminary effort was made to obtain velocity vectors during this experiment. Preliminary vector-fields of particle velocity were obtained using the Insight 3G's ensemble

Table 4: Summary of velocity (vel.) profiles in different microchannel network layers in a PMMA device.

Unit (mm/s)	Min vel.	Max vel.
L _M	0.0	0.0
L _B	0.0	0.0
L _C	0.0	0.37
L _G	0.14	1.47
L _Y	0.14	1.11
L _R	0.14	0.70
L _{LG}	0.14	0.69

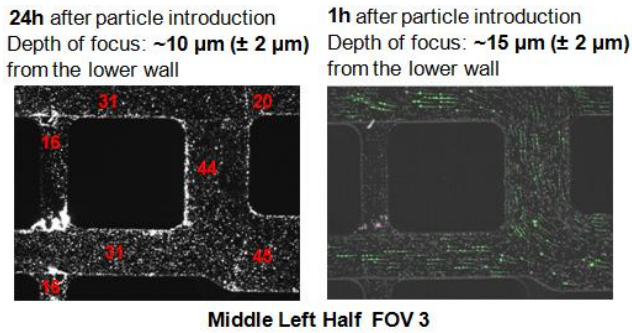


Figure 14: Images from FOV #3 (per Figure 8(a)) from the middle left half region of the 2.5D artificial porous medium micro-model. On the right is an image obtained 1 hr after particle flow was initiated and super imposed to it is a vector field obtained using PIV. On the left is an image obtained 24 hrs after particle flow was initiated. A 10X objective was used to acquire these images with exposure time of 10 ms and image acquisition frequency of 10.753 Hz (left) and exposure time of 20 ms and image acquisition frequency of 9.709 Hz (right). Numbers in red indicate the channel depth.

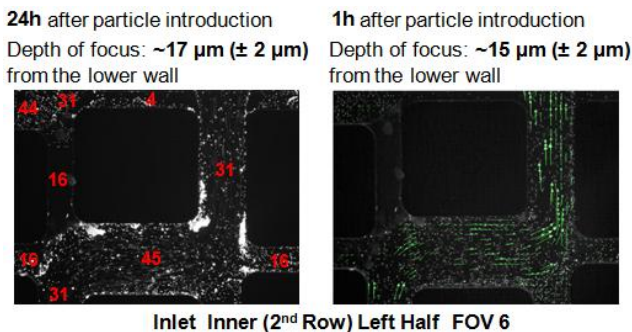


Figure 15: Images from FOV #6 (per Figure 7(a)) from the middle left half region of the 2.5D artificial porous medium micro-model. On the right is an image obtained 1 hr after particle flow was initiated and super imposed to it is a vector field obtained using PIV. On the left is an image obtained 24 hrs after particle flow was initiated. A 10X objective was used to acquire these images with exposure time of 10 ms and image acquisition frequency of 10.753 Hz (left) and exposure time of 20 ms and image acquisition frequency of 9.709 Hz (right). Numbers in red indicate the channel depth.

particle image velocimetry (PIV, TSI Inc., Shoreview, MN, USA) on the micro-scale at a few fields of view from sets of 30 consecutive images acquired at an appropriate sampling rate to resolve a finite velocity range. Each pair of consecutive images renders an instantaneous vector field, and thus 15 vector fields were obtained from the set of 30 acquired images. Averages of these vector fields were computed and a sample of the results is shown in Figures 14 and 15 for a single field of view each. Although, the depth of observation (focal plane location) was measured ($\pm 2 \mu\text{m}$ uncertainty), accurate extraction of velocities on a plane (the focal plane) requires very careful filtering of out-of-focus particles during post-processing. Because the concentration of particles was not optimized for velocity measurement using micro-PIV the results presented may not be highly accurate. Another source of bias is the fact that the range of measurable velocities obtained with fixed measurement parameters is limited ($\sim 0.1 - 1.5 \text{ mm/s}$, Table 4), in a flow where the velocity field is heavily non-homogeneous. Finally, the statistical bias may be high because of the limited size of the sample. Even with these uncertainties regarding quantitative accuracy, the vector fields obtained are representative of the flow paths and directions as is the order of magnitude of the velocities measured during these preliminary experiments.

Knowledge of the particle motion-field coupled with the patterns of particle accumulation can shed some light on the role of the hydrodynamics on this aspect of the problem. For example, in Figure 14 an image of the same FOV showing particle accumulation after 24 hrs of particle flow is shown next to the measured vector field superposed on an image obtained 1 hr after particle introduction. It is evident that particle accumulation on the side-walls of the central blockage structure primarily occurs in the neighborhood of a stagnation corner region and along the corresponding walls, as the flow splits from the wider channel on the right to the two available paths. In addition, accumulation is observed at one end of the narrower and shallower channel ($16 \mu\text{m}$) where particles tend to want to enter, albeit at much lower velocities (below the detection limit) than those encountered in the wider and deeper channels which it connects. Accumulation is also observed in Figure 15 around the neighborhood of stagnation regions located at corners (lower left of the image), as well as at the lower right corner of the principal blockage structure in the image, where the flow and the particles take a sharp bend. In the latter case a low velocity region which favors particle accumulation may exist in that neighborhood, and even a

weak re-circulation depending on the magnitude of the local Dean and Reynolds numbers. These two examples illustrate the need for understanding the local hydrodynamics in order to understand the particle deposition and accumulation processes. Naturally, hydrodynamics are just one part of the physics of the particle deposition/accumulation process. The deposition or adsorption itself is, of-course, controlled to the largest extent by short-range, molecular-level forces between the wall material and the particle, as well as diffusion, once the particle finds itself in regions where the convective effect is sufficiently weak. This makes the problem inherently multi-scale not only at the scales of this experiment, but also when channel (pore) and particle sizes are substantially smaller.

CONCLUSIONS

Microfluidic PMMA devices for artificial porous media were successfully designed and microfabricated using micro-molding, and used for characterization of particle tracking, accumulation, and retention with fluorescent nanoparticles as tracers. Localized particle accumulation and retention occurred more significantly nearer to the inlet section of the PMMA device due to the entrance effect and reduced accumulation and retention observed further downstream, possibly because of dilution of the particle concentration. Deposition and accumulation of particles was correlated to low velocity regions in the channel network such as those occurring at junctions, depth changes, and locations with significant changes in flow direction. Some limited-scope Particle Image Velocimetry in the PMMA device allowed for generating velocity vectors on the micro-scale between 0.1-1.5 mm/s in microchannel network layers. These aided in the interpretation of some of the particle depositions observed.

Further fluidic characterization efforts will provide valuable information to understand the fundamental behavior governing particle transport in complex porous media structures and keys to answer practical questions such as propagation/deposition/retention of particles in real reservoir materials.

ACKNOWLEDGMENTS

This work was supported by the Advanced Energy Consortium (AEC, <http://www.beg.utexas.edu/aec/>). We thank J. Guy at LSU for micromilling of a brass mold insert, the Center for Advanced Microstructures and Devices (CAMD) at LSU for microfabrication support, and Dustin Crandall of the National Energy Technology Laboratory and Goodarz Ahmadi at Mechanical and Aeronautical Engineering, Clarkson University for the original design of the artificial porous medium, which was modified for the purposes of the present study.

REFERENCES

[1] Kampel, G., Goldstein, G. H., and Santamarina, J. C., 2009, "Particle Transport in Porous Media: the Role of Inertial Effects and Path Tortuosity in the Velocity of the Particles", *Applied Physics Letters*, **95**, p. 194103.

- [2] Yoon, J. S., Germaine, J. T., and Culligan, P. J., 2006, "Visualization of Particle Behavior within a Porous Medium: Mechanisms for Particle Filtration and Retardation during Downward Transport", *Water Resources Research*, **42**, p. W0641.
- [3] Andrade, J. S., Almeida, M. P., Filho, J. M., Halvin, S., Suki, B., and Stanley, H. E., 1997, "Fluid Flow through Porous Media: the Role of Stagnant Zones", *Physical Review Letters*, **79**(2), pp. 2901-3904.
- [4] Gaganis, P., Skoiras, E. D., Theodoropoulou, M. A., Tsakiroglou, C. D., and Burganos, V. N., 2005, "On the Evaluation of Dispersion Coefficients from Visualization Experiments in Artificial Porous Media", *J. Hydrology*, **307**, pp. 79-91.
- [5] Crandall, D., Ahmadi, G., and Smith, D. H., 2010, "Computational Modeling of Fluid Flow through a Fracture in Permeable Rock", *Transport in Porous Media*, **84**(2), pp. 493-510.
- [6] Fiorini, G. S. and Chiu, D. T., 2005, "Disposable Microfluidic Devices: Fabrication, Function, and Application", *Biotechniques*, **38**(3), pp. 429-446.
- [7] Heckeke, M. and Schomburg, W. K., 2004, "Review of Micro Molding of Thermoplastic Polymers", *J. Micromech. Microeng*, **14**, pp. R1-R14.
- [8] Hupert, M., Guy, W., Llopis, S., Shadpour, H., Rani, S., Nikitopoulos, D. E., Soper, S. A., 2007, "Evaluation of Micromilled Metal Mold Masters for the Replication of Microchip Electrophoresis devices", *Microfluidics and Nanofluidics*, **3**(1), pp. 1-11.
- [9] Crandall, D., Ahmadi, G., and Smith, D. H., 2009, "Gas-Liquid Channel/Pipe Flows Modeling of Gas-Liquid Flow Through an Interconnected Channel Matrix", ASME FEDSM2009-78092, *11th International Symposium on Gas-Liquid Two-Phase Flows*, Vail, CO.
- [10] Park, D. S., Chen, P.-C., Singh, V., You, B. H., Kim, N., Nikitopoulos, D. E., Soper, S. A., Goettert, J., and Murphy, M. C., 2010, "Titer Plate Formatted Continuous Flow Thermal Reactors for High Throughput Applications: Fabrication and Testing", *J. Micromech. Microeng.*, **20**(5), p. 055003.